Journal of Alloys and Compounds 488 (2009) 469–478

Contents lists available at ScienceDirect

Journal of Alloys and Compounds

journal homepage: www.elsevier.com/locate/jallcom

Experimental study of phase transformation and specific heat of ternary zirconia-based oxides using differential scanning calorimetry

Andrey Zakurdaev*, Xiao Huang

Department of Mechanical and Aerospace Engineering, Carleton University, Ottawa, Ontario, Canada K1S 5B6

ARTICLE INFO

Article history:
Received 15 April 2008
Received in revised form 1 September 2009
Accepted 6 September 2009
Available online 11 September 2009

Keywords:
Ceramics
Sintering
Phase transitions
Thermal analysis

ABSTRACT

Phase transformation and specific heat of five ternary zirconia-based oxides were studied using differential scanning calorimetry (DSC). The ternary oxides were fabricated by doping 7YSZ (3.945 mol.% Y_2O_3–ZrO_2) with pentavalent oxides Ta_2O_5 and Nb_2O_5, trivalent oxides Sc_2O_3 and Yb_2O_3, and tetravalent oxide CeO_2. The addition of pentavalent oxides to 7YSZ increased the formation of monoclinic phase upon cooling in comparison to 7YSZ. The phase transformation from monoclinic phase to tetragonal phase took place in the temperature range of 500–700 °C. The incorporation of trivalent dopants effectively stabilized cubic phase to room temperature; the cubic phase, however, seemed to experience an order to disorder transition during subsequent heating and cooling cycle. Tetravalent oxide addition to 7YSZ increased the formation of tetragonal phase as compared to 7YSZ and no phase transformation was observed between 100 and 1400 °C. The specific heat values for the ternary oxides were measured from room temperature to 1000 °C. The experimentally determined values were compared to that calculated based on the constituent oxides in the system using Neumann–Kopp rule and the discrepancies were further discussed in this study.

1. Introduction

Thermal barrier coatings (TBCs) are used to protect hot section components in modern gas turbine engines. Most of the developments in TBCs have been focused on zirconium oxide ZrO_2 (zirconia) based ceramic materials since they possess lower intrinsic thermal conductivity and better structural properties as compared to other available ceramic materials. However, pure zirconia is rarely used in structural applications due to spontaneous cracking which occurs during phase transformation from high temperature tetragonal (t) phase to room temperature monoclinic (m) phase. Metal oxides (also called dopants) are added to pure zirconia to increase the lattice parameters and subsequently delay or suppress the transformation from tetragonal to monoclinic phase in the ZrO_2 matrix upon cooling [1]. The delayed phase transformation also contributes to the increased toughness of doped ZrO_2 [2] due to transformation toughening. Dopants, such as MgO, CaO, Y_2O_3, Yb_2O_3, and Sc_2O_3, with valence lower than +4 also have the effect of stabilizing the high temperature cubic (c) phases [3]. In addition to phase stabilization, the dopants play a significant role in reducing the thermal conductivity of doped zirconia due to the increased point defect phonon scattering from vacancies, substitutional defects and defect clusters [4–7].

7YSZ (7 wt% or 3.9 mol.% Y_2O_3 stabilized ZrO_2), the most successfully developed TBC material, assumes a metastable tetragonal t'-phase when rapidly cooled from the high temperature cubic phase region to room temperature. This t'-phase exhibits high toughness and superior high temperature durability than the others [8]. Prolonged high temperature exposure has been reported to result in a thermal conductivity increase due to sintering effect in reducing the porosity [9]. Furthermore, the tetragonal t'-phase in 7YSZ decomposes to yttria-poor tetragonal and yttria-rich cubic phases upon extended exposure at temperatures above 1200 °C. On cooling, the yttria-poor tetragonal phase will transform into m-phase, resulting in coating cracking [10,11].

To improve the phase stability of binary YSZ TBC system at high temperatures, the addition of co-doping oxides and the use of multiple oxide dopants are being considered. It has been found that when two dopant oxides, Nd_2O_3 (or Gd_2O_3) and Yb_2O_3 (or Sc_2O_3), are added to ZrO_2 (or HfO_2), a thermodynamically stable, highly defective lattice structure can be obtained [12]. In this type of structure, point defect clusters and nanoscale ordered phases have been found. Compared with a binary system such as YSZ, these multiple oxides doped zirconia systems exhibit more stable microstructure at high temperatures and lower thermal conductivity at the same time [13].

To overcome the disadvantages associated with the YSZ based TBC materials, new TBC materials will likely be formulated using a

* Corresponding author. Tel.: +1 613 520 2600; fax: +1 613 520 5715.
E-mail address: xhuang@mae.carleton.ca (A. Zakurdaev).

0925-8388/$ – see front matter © 2009 Elsevier B.V. All rights reserved.
doi:10.1016/j.jallcom.2009.09.013

Table 1
Characteristics of selected metal oxides as co-dopant to 7YSZ.

Dopant	Dopant cation	Atomic mass of the cation	Ionic radius of the cation (nm)
Y_2O_3	Y^{3+}	88.91	0.089
Ta_2O_5	Ta^{5+}	180.95	0.068
Nb_2O_5	Nb^{5+}	92.91	0.069
Sc_2O_3	Sc^{3+}	44.96	0.072
Yb_2O_3	Yb^{3+}	173.04	0.086
CeO_2	Ce^{4+}	140.11	0.092
(ZrO_2)	Zr^{4+}	91.22	0.079

complex, higher order oxide system, to provide improved thermal stability and reduced thermal conductivity. In this study, several ternary oxide systems, formulated by co-doping YSZ, were evaluated. A systematic approach was used to select the co-dopants based on the valence of the co-dopant cation, atomic mass, and cation radius. The influences of various co-dopants on the initial microstructure, phase transformation and heat capacity of YSZ were evaluated.

2. Experimental procedures

2.1. Materials and fabrication methods

7YSZ (3.945 mol.% Y_2O_3–ZrO_2) was selected as the base material in this study. The pentavalent oxides Ta_2O_5 and Nb_2O_5, with similar cation ion radius but different atomic mass, were added to 7YSZ in equal molar percentage of Y_2O_3 in order to annihilate the oxygen vacancies in 7YSZ. The trivalent dopants Sc_2O_3 and Yb_2O_3, with substantial difference in their atomic mass, were selected to create substitutional point defects by replacing Zr^{4+} in the lattice structure and extra oxygen vacancies. Additionally, tetravalent oxide CeO_2 was added to 7YSZ to examine the effect of substitutional defects only since no extra oxygen vacancies can be created with tetravalent CeO_2 addition. Both trivalent and tetravalent co-dopants were added to result in 12 mol.% of total dopant cations. For comparison purposes, 7YSZ was also included in the study. Table 1 lists the characteristics of co-doping oxides used in this study and Table 2 gives the actual molar fraction of the co-dopant additions.

Oxide powder materials were blended according to the compositions given in Table 2 and milled using a ball-milling machine. The ball-milling method was selected to alloy the powder material since it is simple, effective and has shown success in achieving complete solid solution after 24-h milling time [14,15]. ZrO_2 balls with density of 6.27 g/cm^3 and ball diameter of 10 mm were used as the grinding media. After ~20 h milling, the alloyed powders were compacted uniaxially at 200 MPa to form 2–4 mm thick and 15 mm diameter discs. A sintering process at 1500 °C for 120 h was used to consolidate the green compact and homogenize the compositions. The sintering time of 120 h was estimated based the diffusion of cations at 1500 °C for a distance of ~7 μm [16] as the largest powder particle size after ball-milling was found to be ~15 μm. After sintering, the samples were furnace cooled to room temperature at a cooling rate of ~5 °C/min.

2.2. Microstructure study and determination of phase composition

A scanning electron microscope (SEM) (Hitachi S-570 SEM) was employed in this study to evaluate the surface morphologies of the sintered samples. A Rigaku™ XRD with a Cu K_α radiation source (λ = 0.1542 nm) was used to determine the phase compositions in the sintered samples. Each scan was carried out over the 2θ range of 20–100° at a scan rate of 0.8°/min. The phase compositions for various samples were determined by comparing the X-ray diffraction (XRD) pattern of the sample with a reference database of crystalline phases. The percentages of various phases were calculated using relative integrated intensity of the characteristic X-ray diffraction peaks as detailed in references [17,18].

Table 2
Compositions of Dopant Cations in 7YSZ.

Sample ID	Co-doping oxide (mol%)	Co-dopant cation		Y^{3+} (mol%)
		(wt%)	(mol%)	
7TaYSZ	3.945 mol.% Ta_2O_5	12.03	7.05 (Ta^{5+})	7.06
7NbYSZ	3.945 mol.% Nb_2O_5	7.60	7.05 (Nb^{5+})	7.06
5ScYSZ	5 mol.% $ScO_{1.5}$	2.71	4.71 (Sc^{3+})	7.23
5YbYSZ	5 mol.% $YbO_{1.5}$	7.37	4.71 (Yb^{3+})	7.23
5CeYSZ	5 mol.% CeO_2	6.50	4.71 (Ce^{4+})	7.23

2.3. Differential scanning calorimetry (DSC)

To observe the phase transformation of the sintered materials during subsequent heating and cooling, thermal analysis was performed using heat flux differential scanning calorimetry (DSC), a technique which involves the detection of changes in thermal energy (enthalpy) or specific heat of a sample with temperature.

In heat flux DSC, the test sample and an inert reference material (pure alumina) are placed in alumina crucibles located in the same furnace. The thermocouple junctions are attached to the individual conducting bases where the crucibles are positioned, preventing direct contact between the thermocouples and sample or reference material. In order to maintain identical temperature for the sample and reference material during heating or cooling, different heat flux is required since the specific heat values for the sample and reference materials are different. The relationship of differential heat flux versus temperature is recorded and known as a DSC thermogram (curve). Any transition associated with absorption or generation of heat causes a discontinuity in the heat flux and results in a peak on the DSC curve. An exothermic process is represented by an upward deviation from the baseline, while a downward deflection indicates the onset of an endothermic reaction. The onset, peak and end temperatures for the phase transformation can be determined from the DSC curve based on this principle.

In each DSC run in this study, the same temperature cycle was followed. The cycle began in the initial standby from room temperature up to 100 °C at 15 °C/min. This initial standby portion of the run ensured that all tests began under the same condition. Next, the temperature was increased from 100 °C to 1400 °C at a heating rate of 20 °C/min. Then, the samples were isothermally held at 1400 °C for 5 min, after which the temperature was decreased to 200 °C at a cooling rate of 50 °C/min. After performing several initial tests, it was found that the apparatus stopped recording upon reaching 400 °C during cooling. As such, all DSC heat flux measurements during the cooling cycle were terminated at 400 °C.

A Netzsch DSC 404C Pegasus heat flux calorimeter (Netzsch-Geratebau GmbH, Germany) was used in this study. Heating and cooling were controlled through a TASC 414/4 controller (Netzsch-Geratebau GmbH, Germany) linked to a PC based Proteus software. During the heat flux DSC tests, a high purity argon atmosphere with a flow rate of 60 mL/min was used.

2.4. Specific heat measurement

The principle for measuring the specific heat of the test sample using DSC is based on the following equation:

$$C_{p,\text{sample}} = \frac{m_{\text{standard}}}{m_{\text{sample}}} \cdot \frac{DSC_{\text{sample}} - DSC_{\text{baseline}}}{DSC_{\text{standard}} - DSC_{\text{baseline}}} \cdot C_{p,\text{standard}} \quad (1)$$

where $C_{p,\text{sample}}$ is the specific heat of the sample at temperature T; $C_{p,\text{standard}}$ is the known standard specific heat of the standard (sapphire) at temperature T; m_{sample} and m_{standard} are the masses of the sample and sapphire, respectively; and DSC_{sample}, DSC_{standard}, and DSC_{baseline} are the values of the heat flux signal at temperature T from the sample, sapphire, and baseline curves, respectively [19,20]. In this study, the specific heat measurement was only conducted during the heating cycle at a heating rate of 20 °C/min.

As indicated in Eq. (1), three measurements are required to obtain the specific heat values of the test sample: (1) a baseline measurement performed by running heat flux DSC using an empty sample crucible and a reference crucible with reference material (pure alumina disc); (2) a standard measurement using a sapphire disc as a standard sample in the sample crucible; and (3) the actual sample measurement with reference material and sample material.

Prior to running the actual measurement, calibration was carried out by testing pure metallic samples (In, Sn, Al, Au and Ni) with known melting temperatures and enthalpy to obtain a calibration curve, which corrects the temperatures and enthalpy measured by the instrument, as a function of instrument temperature. For each calibration run, an appropriate heating program was selected to heat the pure metallic sample at 20 °C/min to just above the melting temperature, in addition to a baseline run for each particular heating program. Two heating cycles were used, and their results were averaged as the input for the calibration file. Temperature calibration used the melting temperatures of pure samples taken at the onset temperature on the DSC curve where melting just began while enthalpy calibration used the area under the melting peaks of the heat flux DSC curves.

During test, the following parameters were kept constant: atmosphere in the measuring cell, argon flow rate, initial temperature, heating rate and scanning rate, mass of crucible and lid, and the position of crucible in the cell.

2.5. Sample preparation

The weight of the tested samples was measured to be 35–45 mg and the sample dimension was less than that of the crucibles so as to be fully contained within the crucible. For the heat flux DSC experiments and specific heat measurements, the samples and reference material were held in high purity alumina (Al_2O_3) crucibles. An alumina disc, of weight 41.2 mg, was used as the reference material for all tests. Prior to each run, both crucibles were thoroughly rinsed with acetone and blow-dried with compressed air. The masses of the crucibles were also recorded before and after every test to detect any contamination from possible chemical reactions.

Table 3
The relative content of *m*- and *c*-, *t*-phases determined from XRD.

Sample ID	Experimental results from XRD	
	mol.% of *m*-phase	mol.% of *c* + *t*-phase
7YSZ	46	54 (*c*)
7TaYSZ	100	0
7NbYSZ	97	3 (*t*)
5ScYSZ	6	94 (*c*)
5YbYSZ	–	100 (*c*)
5CeYSZ	2.5	97.5 (*c* + *t*)

3. Results

3.1. Microstructure analysis

The microstructures of the as-sintered materials were examined using SEM using as-polished specimens. As shown in Fig. 1, the 7NbYSZ and 5CeYSZ exhibited adequate consolidation after 120-h sintering at 1500 °C. This was indicated by well-defined grain structure on the polished surface and limited porosity. In samples with compositions of 7YSZ and 7TaYSZ, increased porosity was observed as compared to that of 7NbYSZ and 5CeYSZ. A more porous structure was observed for samples 5ScYSZ and 5YbYSZ. While the existence of porosity has significant effect on the thermal conductivities of ceramic materials, it was not observed to have any impact on the specific heat measurements [21]. As such, the results on the porosity measurements were not included here.

The phase compositions of the sintered ceramic materials were further characterised by X-ray diffraction (XRD) with the results summarized in Fig. 2 and Table 3 and. Pure zirconia can assume three different crystal structures, namely monoclinic (*m*), tetragonal (*t*) and cubic (*c*) phases, depending on the temperature. The addition of dopant and co-dopant had a significant impact on the microstructure, as observed in this study. The XRD results showed that the sintered 7YSZ contained 46 mol.% *m*-phase and 54 mol.% *c*-phase at room temperature, while 7TaYSZ and 7NbYSZ contained 100 mol.% and 97 mol.% *m*-phase, respectively. Unlike that in the conventionally thermal sprayed 7YSZ where 100% *t*′-phase was achieved due the faster cooling rate from higher temperature (100% *c*-phase region), sintered 7YSZ contained substantial *m*-phase as sintering process was carried out in the two-phase region (*c* + *t*). Upon cooling the *t*-phase would transform into *m*-phase. An additional 3 mol.% *t*-phase remained in the sample of 7NbYSZ after cooling from sintering temperature. Ternary phase diagrams [22,23] showed that both 7TaYSZ and 7NbYSZ assume single *t*-phase at the sintering temperature of 1500 °C. The additions of pentavalent Ta_2O_5 and Nb_2O_5 to 7YSZ suppressed the oxygen vacancy and promoted the occurrence of *t*-phase at the sintering temperature of 1500 °C. This *t*-phase was subsequently transformed into *m*-phase during cooling. Nb_2O_5, with smaller cation mass than Ta_2O_5, seemed to have more stabilization effect on high temperature *t*-phase. Further results from heat flux DSC confirmed this observation.

In 5ScYSZ, cubic phase comprised the majority of the phase composition, with a small amount of *m*-phase (6 mol.%); while 5YbYSZ contained 100 mol.% *c*-phase. Finally, in sample 5CeYSZ, the presence of a small amount of *m*-phase (2.5 mol.%) was found, with the remainder consisting of a mixture of *t*-phase and *c*-phase (97.51 mol.%). Detailed analysis on the effects dopants, grain size and porosities were reported in Ref. [24].

3.2. DSC analysis of phase transformation

To study the phase transformation and stability of the sintered materials during subsequent heating and cooling, heat flux DSC analysis was carried out on five ternary oxides and 7YSZ.

From the XRD results summarized in Table 3, 7YSZ contained 46 mol.% *m*-phase in addition to 54 mol.% of *c*-phase. Observing the heat flux DSC curve for 7SYZ in Fig. 3, a phase transformation took place at 621 °C (onset temperature) during heating as indicated by the change in heat flux from the baseline. Since the low temperature *m*-phase is unstable at higher temperature, the observed phase transformation can be identified as $m \rightarrow t$ transition. This is consistent with that predicated from the binary ZrO_2–Y_2O_3 binary phase diagram where a transition from $m \rightarrow t$ occurs at ~600 °C [25]. With a further increase in temperature, the DSC curve did not exhibit any peak up to 1400 °C. During the cooling cycle at a rate of 50 °C/min, a phase transformation corresponding to $t \rightarrow m$ was observed at 483 °C (onset temperature). This phase transformation

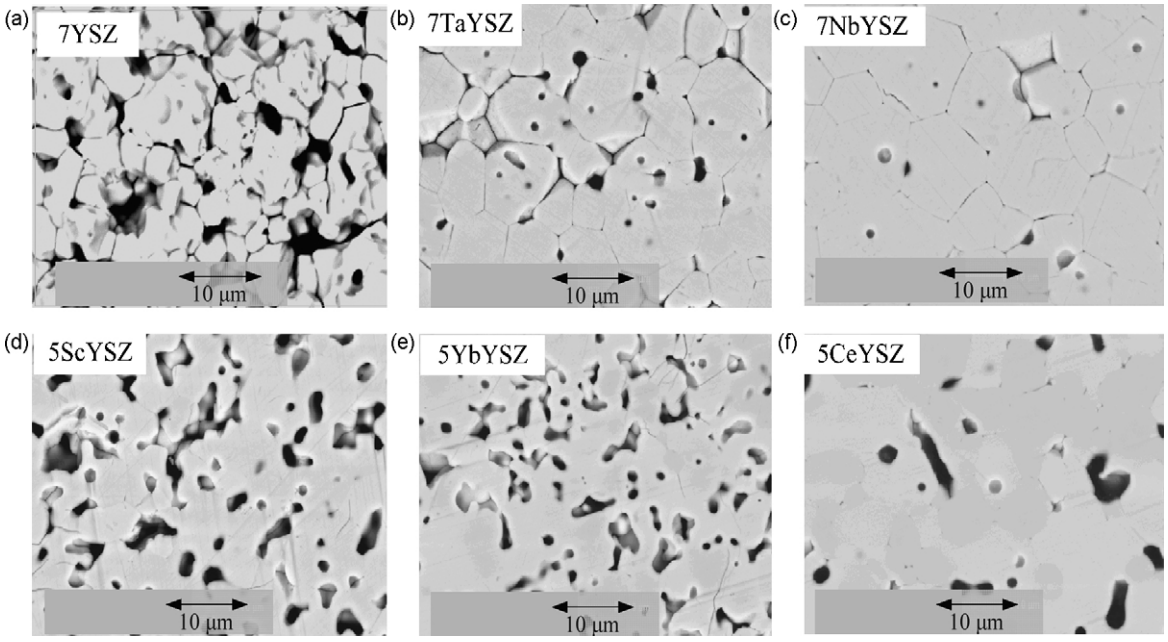

Fig. 1. Microstructure of the as-polished sintered specimens (a–f).

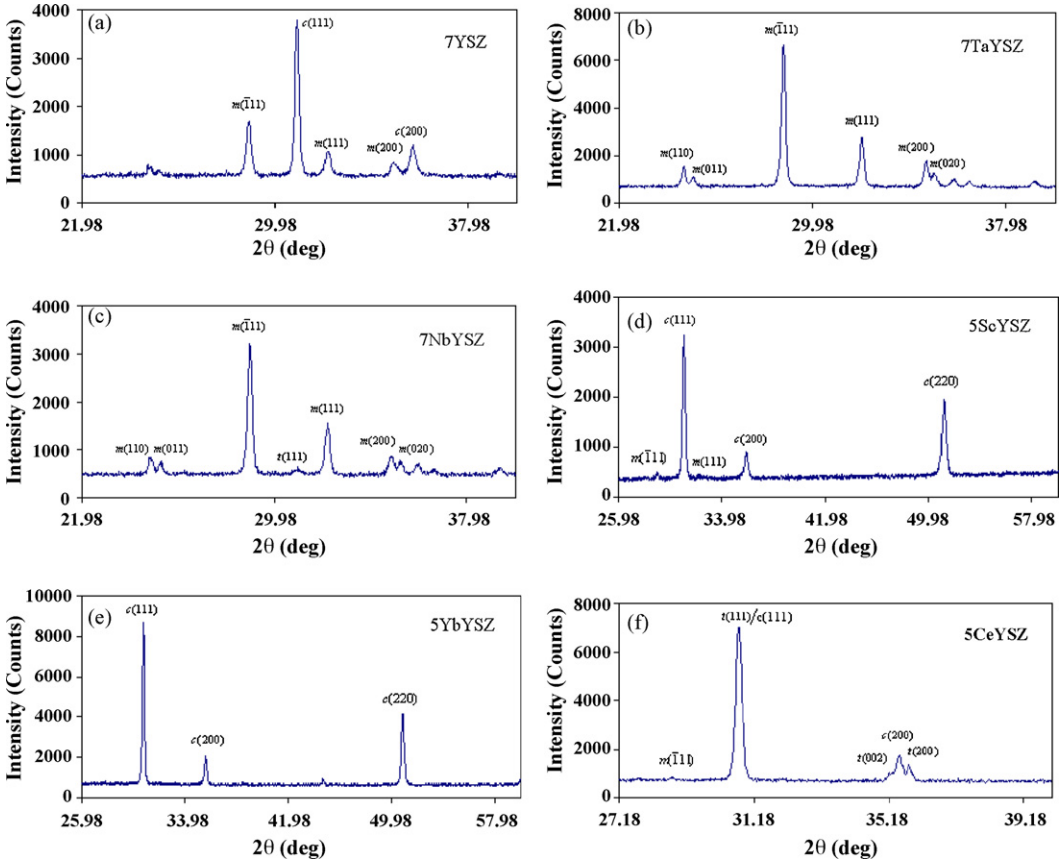

Fig. 2. XRD patterns for (a) 7YSZ, (b) 7TaYSZ, (c) 7NbYSZ, (d) 5ScYSZ, (e) 5YbYSZ, and (f) 5CeYSZ.

temperature is much lower than observed on the heating cycle due to undercooling.

The heat flux DSC curves for 7TaYSZ and 7NbYSZ are shown in Fig. 4(a) and (b), respectively. Upon heating, 7TaYSZ, with 100 mol.% *m*-phase after sintering, displayed a phase transformation at 632 °C (onset temperature). The ZrO_2–Y_2O_3–Ta_2O_3 ternary phase diagram indicates that 7TaYSZ assumes single *t*-phase at 1500 °C [22]. As such, the observed peak at 632 °C should correspond to $m \rightarrow t$ phase transformation. During cooling, a phase transformation took place at 522 °C (onset temperature) suggesting a reversed transformation of $t \rightarrow m$. For sample 7NbYSZ, the transformation from $m \rightarrow t$ appeared at a much lower temperature of 524 °C (onset) as shown in Fig. 4(b). And when the temperature was further increased, another small deviation from the baseline was observed after reaching 570 °C. This split peak has been observed previously during DSC analysis by other researchers [26]. It was believed that the $m \rightarrow t$ phase transformation may cause a "burst" reaction due to the nature of martensitic phase transformation [27]. Unlike 7TaYSZ,

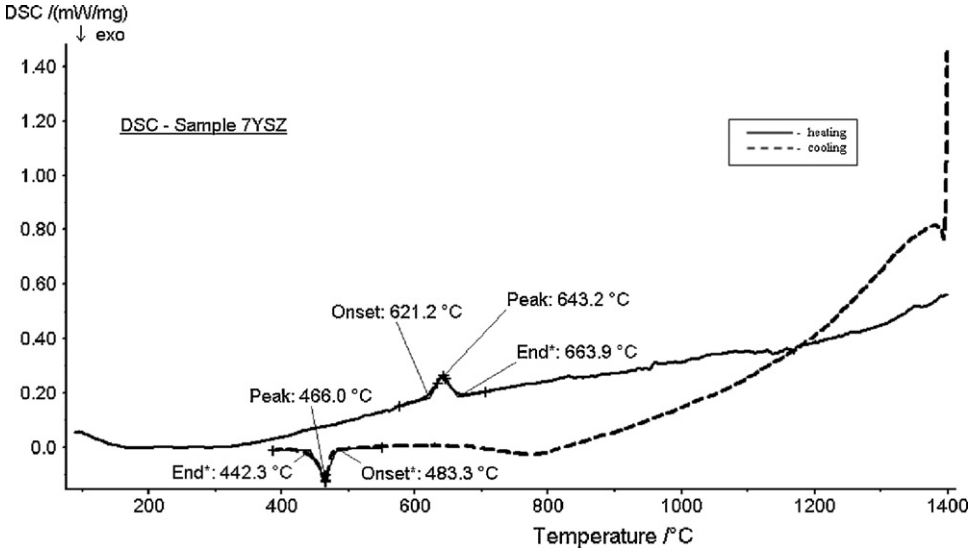

Fig. 3. DSC curves for 7YSZ.

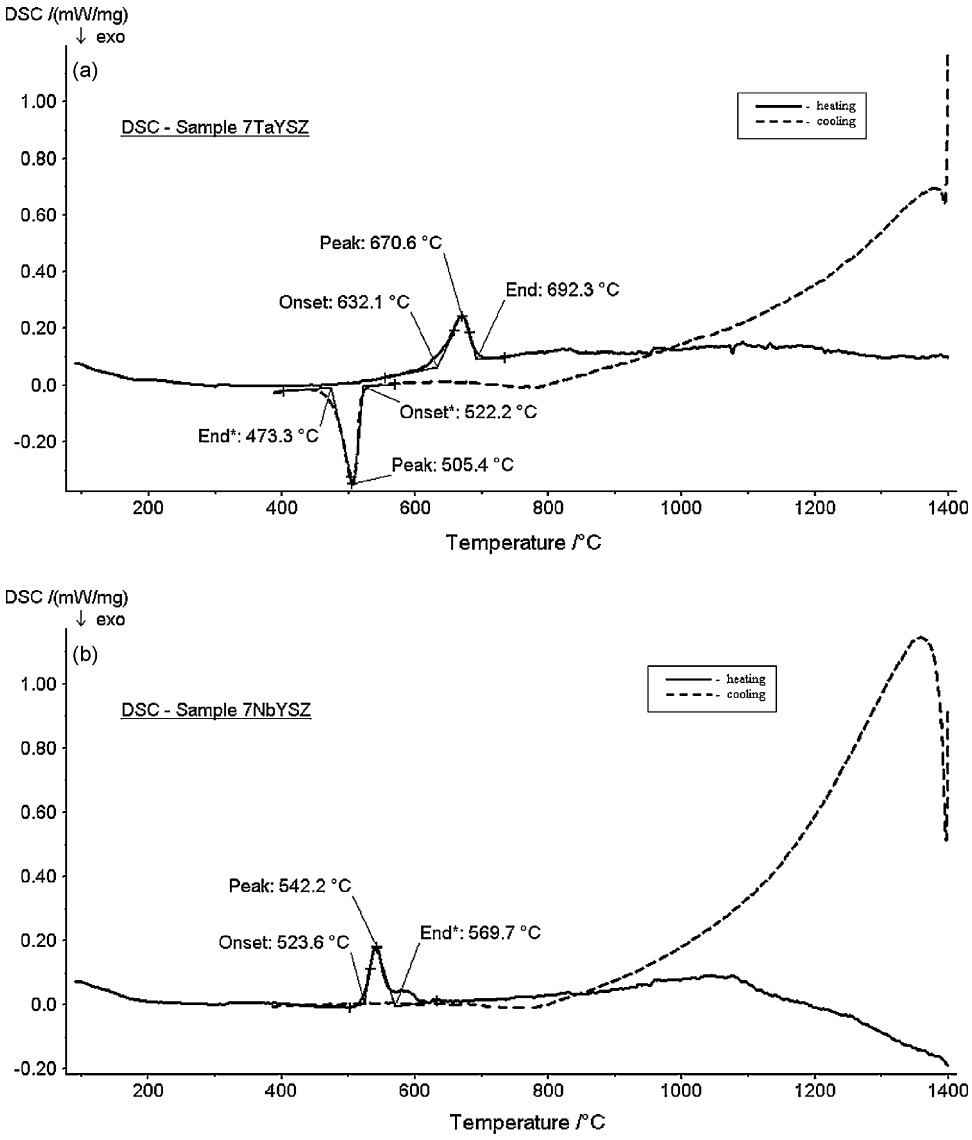

Fig. 4. DSC curves for (a) 7TaYSZ and (b) 7NbYSZ.

7NbYSZ did not show the phase transformation of $t \rightarrow m$ before 400 °C during cooling, indicating the effect of Nb_2O_5 in lowering the Ms temperature for $t \rightarrow m$ in 7NbYSZ.

The DSC curves for samples 5ScYSZ and 5YbYSZ are shown in Fig. 5(a) and (b). As determined from XRD analysis, samples 5ScYSZ and 5YbYSZ contain 94 mol.% and 100 mol.% *c*-phase, respectively. During the heating cycle, there was no apparent phase transformation observed on the heat flux DSC curves for both samples even though 5ScYSZ contained 6 mol.% of *m*-phase after sintering. The absence of $m \rightarrow t$ transformation on the DSC curve for 5ScYSZ can be attributed to either limited instrument sensitivity or the stable nature of the *m*-phase surrounded by *c*-phase. Upon cooling, however, a noticeable endothermic reaction in the temperature range of 1300–600 °C was observed in both samples. Since only samples with trivalent dopant and co-dopant and substantial *c*-phase (5ScYSZ and 5YbYSZ) exhibited the endothermic reaction, it is believed that this reaction may be associated with defect clustering/ordering during cooling. In fact, it has been observed in other research that the oxygen vacancies in *c*-phase preferentially locate on the next nearest neighbour to the substitutional dopant cations such as Y^{3+} (Sc^{3+} and Yb^{3+}) forming highly localized oxygen-cation clusters [28–30]. Upon reheating to a critical temperature, rapid diffusion of oxygen anions may occur producing a disordered structure [31]. Thus, the endothermic reaction shown in Fig. 6(a) and (b) was caused by the occurrence of defect ordering over a large temperature range during cooling. It is not clear why the transition from ordered to disordered *c*-phase was not observed during the heating cycle of the DSC curve.

Sample 5CeYSZ contained primarily *t*- and *c*-phases and a small amount of *m*-phase (2.5 mol.%) (Table 3). Unlike 7YSZ, most of the *t*-phase in 5CeYSZ formed at sintering temperature was effectively stabilized to room temperature due to the addition of CeO_2. Dopants with larger ionic radius (such as Ce^{4+}) relative to that of Zr^{4+} have been found to stabilize *t*-phase to a lower temperature [32]. The mechanism of the stabilization can be attributed to the reduction in Ms temperature for $t \rightarrow m$-phase [33]. The stabilization effect of CeO_2 became evident by observing the DSC curve shown in Fig. 7 where no phase transformation was detected during both heating and cooling. While the stabilization effect of CeO_2 on *t*-phase was confirmed by both XRD and DSC analyses in this study, it is also interesting to note that despite the stabilization of *t*-phase by CeO_2 addition, there was still 2.5 mol.% *m*-phase existing in the sample after sintering. The monoclinic phase could have formed on the free surfaces (external and internal pore surfaces

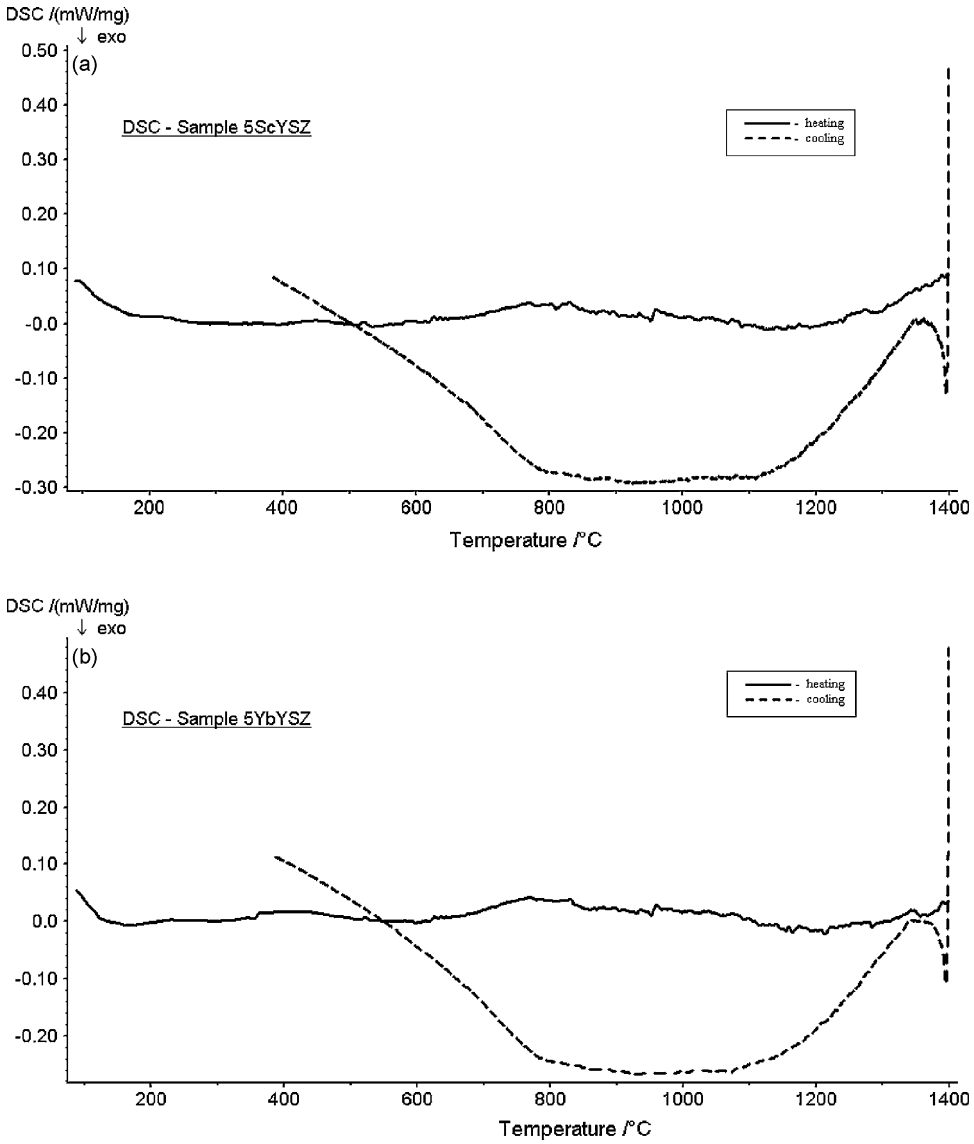

Fig. 5. DSC curves for (a) 5ScYSZ and (b) 5YbYSZ.

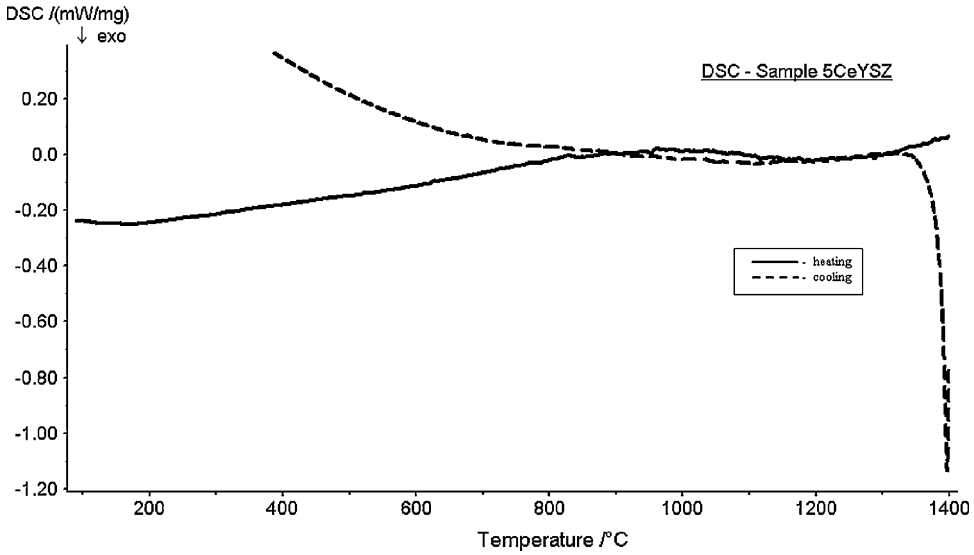

Fig. 6. DSC curves for 5CeYSZ.

during cooling) as 5CeYSZ contained about 5 vol.% of porosity after sintering. The occurrence of *m*-phase in a porous structure has been attributed to the reduction in free energy (strain energy and surface energy) associated with *m*-phase formation on the free surfaces as $t \rightarrow m$ accompanies volume increase [2,33]. It is not certain at present whether the 2.5 mol.% of *m*-phase in 5CeYSZ had transformed to *t*-phase upon heating since the detection limit of the heat flux DSC is unknown.

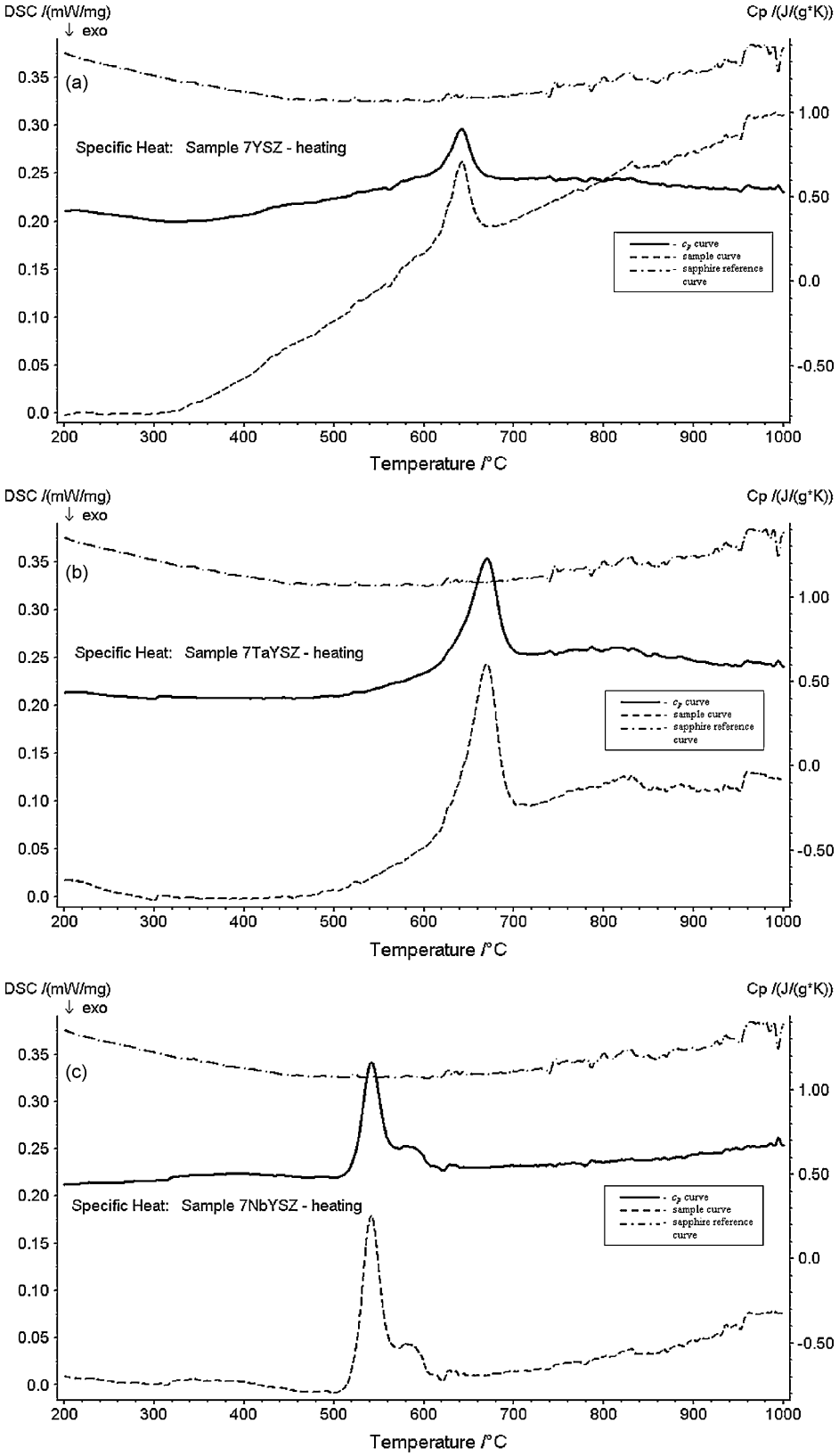

Fig. 7. (a) C_p curve for 7YSZ (heating), (b) C_p curve for 7TaYSZ (heating), (c) C_p curve for 7NbYSZ (heating), (d) C_p curve for 5ScYSZ (heating), (e) C_p curve for 5YbYSZ (heating), and (f) C_p curve for 5CeYSZ (heating).

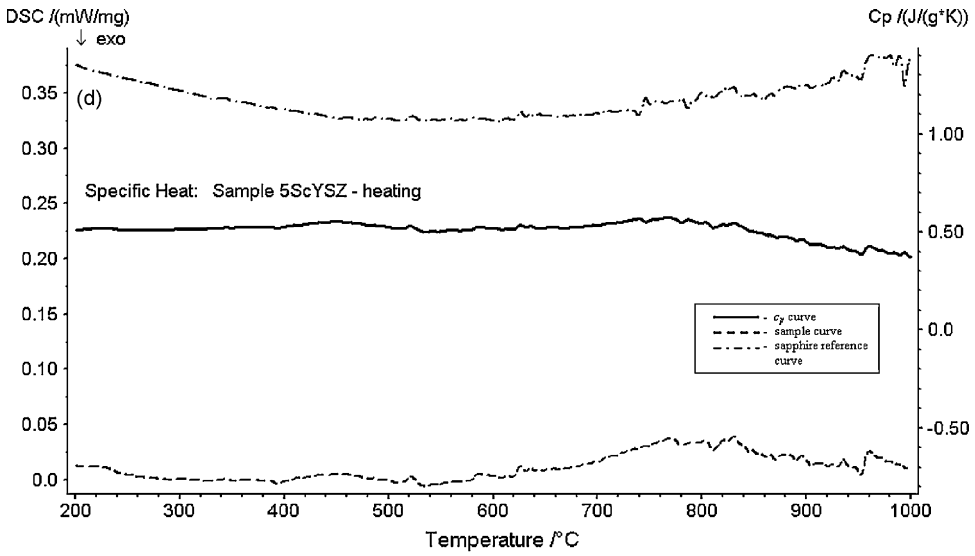

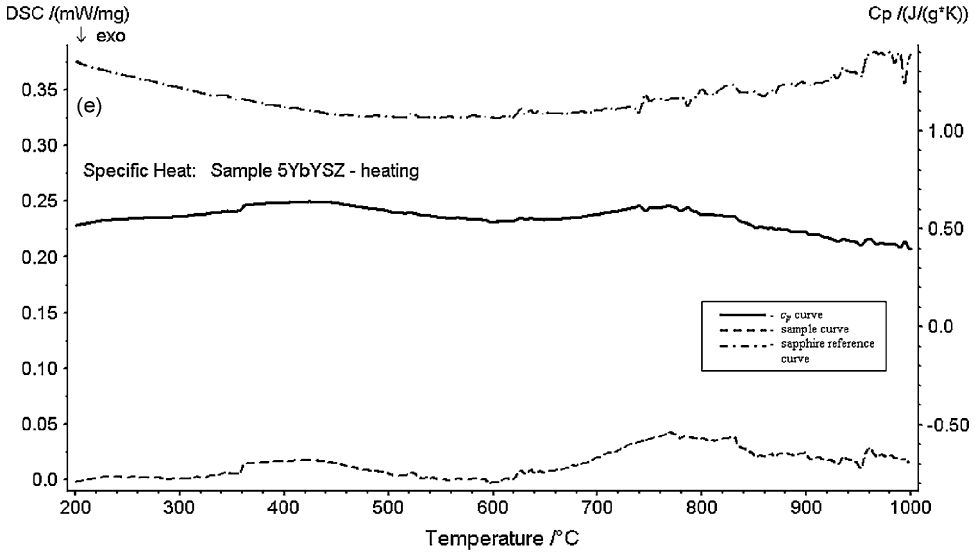

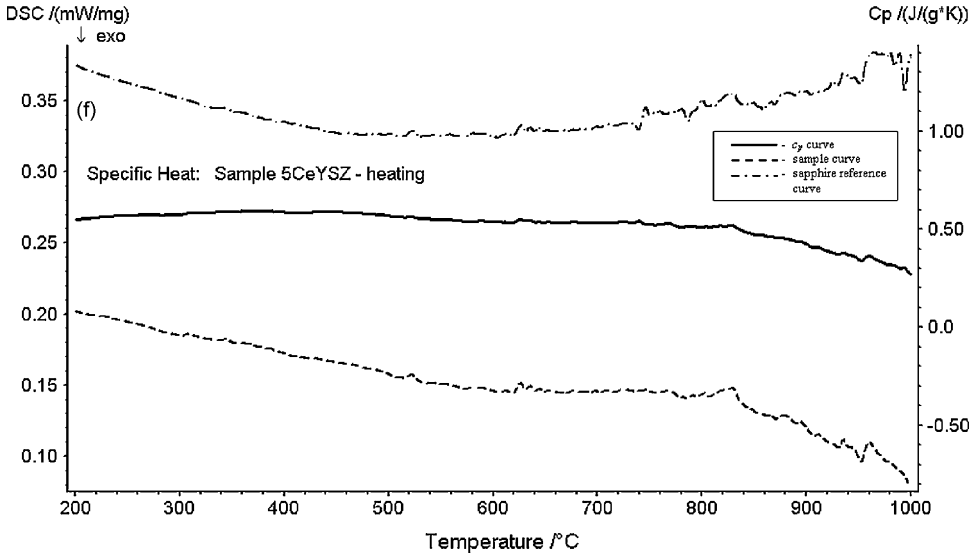

Fig. 7. (*Continued*).

Table 4
Experimentally measured specific heat values (heating).

Sample	Specific heat, C_p (J/kg K)						
	200 °C	300 °C	400 °C	500 °C	600 °C	700 °C	800 °C
7YSZ	414	460	480* −17%	487	(618)	(606)	586
7TaYSZ	431	392	400* −25%	413	(547)	(685)	675
7NbYSZ	436	460	502* −14%	(478)	(610)	551	565
5ScYSZ	507	512	523* −10%	(522)	(518)	(531)	(536)
5YbYSZ	513	560	632* 16%	(587)	(532)	(574)	(571)
5CeYSZ	547	572	585* 3%	566	536	533	503

* The difference between experimentally measured and the calculated values.

3.3. Specific heat

The specific heat (C_p) values of the samples were measured following the procedures detailed in Section 2. The C_p values as a function of temperature (from 200 to 1000 °C) during heating cycle are presented in Fig. 7(a)–(f) for the six samples studied. Also included in each figure is the DSC heat flux curve of the same sample to help identify the temperatures at which phase transformation occurs. Table 4 provides a summary of the measured specific heat values extracted from Fig. 7 for the temperature range of 200–800 °C. The specific heat values enclosed in brackets in Table 4 were measured within the temperature region where phase transformation occurred. These values were affected by the heat generation or absorption accompanied the phase transformation and could not be used to represent the true specific heat capacities.

For sample 7YSZ, the C_p curve showed an increasing trend from about 400 °C up to the onset temperature of 621 °C where the phase transformation of $m \rightarrow t$ took place. Upon the completion of phase transformation, it seemed to follow a gradual decreasing trend as shown in Fig. 7(a). The C_p curves for samples 7TaYSZ and 7NbYSZ, Fig. 7(b) and (c), showed steady values prior to the occurrence of $m \rightarrow t$ transformation at 632 °C and 524 °C, respectively. Upon the completion of phase transformation, the C_p values for 7TaYSZ followed a similar behaviour as 7YSZ, while 7NbYSZ showed a gradually increasing trend up to 1000 °C. The nature of the slit peaks for sample 7NbYSZ has been discussed in the DSC analysis of phase transformation.

The C_p curves for samples 5ScYSZ and 5YbYSZ are shown in Fig. 7(d) and (e) respectively. Both displayed quite stable C_p values as a function of temperature. By carefully observing the curves, the C_p values seemed to reach a localized peak around 800 °C; this could indicate possible order to disorder transition for the *c*-phase that was not revealed clearly from DSC curves during heating cycle. Lastly, for sample 5CeYSZ, Fig. 7(f), the C_p curve showed an increasing trend up to 800 °C which was then followed by a slight decline from 800 to 1000 °C.

3.4. Comparison between calculated and experimentally determined specific heat values

The specific heat, in particular at high temperature, depends on the nature of the dopants [34]. According to Neumann–Kopp rule [35,36], the specific heat of a gram-atom of a solid compound can be determined using the weighted sum of the heat capacity of the elements forming the compound:

$$(C_p)_{A_xB_yC_z} = x(C_p)_A + y(C_p)_B + z(C_p)_C \quad (2)$$

where the *x*, *y* and *z* are molar fractions of the elements *A*, *B* and *C*, respectively, in compound $A_xB_yC_z$. Using this relationship, the specific heat values for the six samples examined in this study can be determined based on the chemical compositions and the specific heat data of the constituent oxides at various temperatures.

From the information given in the literature [35–37], the specific heat values of ZrO_2, Y_2O_3, Ta_2O_5, Nb_2O_5, Sc_2O_3, Yb_2O_3 and CeO_2 can be estimated using:

$$C_p = A + B \times 10^{-3}T + C \times 10^5/T^2 (\text{cal/mole K}) \quad (3)$$

where *T* is temperature in K. The values of *A*, *B* and *C* for the oxides ZrO_2, Y_2O_3, Ta_2O_5, Nb_2O_5, Sc_2O_3, Yb_2O_3 and CeO_2 are summarized in Table 5. Using Eqs. (2) and (3) and the information from Table 5, the specific heat values for 7YSZ, 7TaYSZ, 7NbYSZ, 5ScYSZ, 5YbYSZ and 5CeYSZ at temperatures of 200, 400, 600, and 800 °C were calculated and given in Table 6. The molar fractions of dopant (Y_2O_3) and co-dopants and molecular weight of the co-doping oxide are also included in Table 6. The unit cal/mole K employed in Eq. (3) was converted to J/kg K in Table 6 to be consistent with the experimentally measured specific heat values.

Comparing the experimentally determined specific heat values given in Table 4 with the calculated ones in Table 6, discrepancies were observed to vary from sample to sample and with temperatures. For example, the discrepancies were 3% and 25% at 400 °C for samples 5CeYSZ and 7TaYSZ, respectively. These can be attributed to the several factors. First, since five specimens (except 5CeYSZ) examined this study experienced phase transformation (7YSZ, 7TaYSZ and 7NbYSZ) or possible order to disorder transition (5ScYSZ and 5YbYSZ) in the temperature range studied, considerable errors for the C_p values measured in vicinity of the onset and end transformation temperatures can be resulted. Even with the completion of the detected phase transformation, the phase compositions will continue to change with the temperature in order to adjust to the equilibrium state thus affecting the specific heat measurements for samples containing multiple phases.

Secondly, the instrument calibration procedure used in this study to determine the specific heat also contributed to certain experimental errors. The calibration of temperature and enthalpy using pure metals was carried out in this study with five samples of different melting temperatures (In, Sn, Al, Au and Ni with melting temperatures from 156 to 1455 °C). A continuous temperature calibration curve as a function of instrument temperature was generated from these five data points utilizing interpolation. The use of limited number of pure metals for calibration increased the inaccuracy in specific heat measurement. Additionally, a high heating rate of 20 °C/min. was used in this study; the fast heating rate and the low thermal conductivity of the samples may not allow the samples to reach the set temperature uniformly leading to inaccurate temperature and heat flux measurements. Further more, since flowing argon was used during DSC tests, the low partial pressure of oxygen in the environment may cause reduction or dissociation of the oxides at high temperature. This chemical reaction, if occurred, was minimal as the weight changes of the samples before and after testing fell below 0.3%.

Additionally, as the coefficients *A*, *B* and *C* in Eq. (3) for the calculation of specific heat of various oxides as a function of temperature were experimentally determined, this could contribute to error in the calculated specific heat values. As well, the calculation of the theoretical specific heat values using Eq. (2) did not take into consideration of the phase compositions. While it has been reported

Table 5
Coefficients used to calculate the specific heat [35,37].

	A	*B*	*C*
ZrO_2	16.64	1.8	−3.36
Y_2O_3	27.27	4.63	−3.68
Ta_2O_5	37	6.56	−5.92
Nb_2O_5	38.76	3.54	−7.32
Sc_2O_3	23.17	5.64	0
Yb_2O_3	30.75	4.65	−4.1
CeO_2	15.49	4.23	−1.815

Table 6
Calculated specific heat values.

Sample	Mole fraction of dopant and co-dopant				C_p values at various temperature (°C) (J/kg K)			
	Y_2O_3	ZrO_2	Co-dopant	Molecular weight (g/mole)	200	400	600	800
7YSZ	0.076	0.924		131	539	577	599	617
7TaYSZ	0.0706	0.8589	0.0705 (Ta_2O_5)	153	502	536	558	576
7NbYSZ	0.0706	0.8589	0.0705 (Nb_2O_5)	141	545	583	605	622
5ScYSZ	0.0723	0.8806	0.0471 (Sc_2O_3)	133	543	579	602	620
5YbYSZ	0.0723	0.8806	0.0471 (Yb_2O_3)	143	512	547	569	586
5CeYSZ	0.0723	0.8806	0.0471 (CeO_2)	133	531	568	591	609

that no significant difference was observed between the specific heat values for *m*- or *t*-phase of pure zirconia [26], the changes in the distributions of dopant and co-dopant in different phases may impact the specific heat values of binary or ternary oxides with multiple phases.

4. Conclusion

In this study, five ternary oxides were formed by co-doping 7YSZ with different oxides. Mechanical alloying and high temperature sintering were used to achieve powder material consolidation and solid solution of co-doping oxides. The microstructure of the sintered material was evaluated using XRD to determine the initial phase compositions prior to DSC analysis. The phase transformation of the sintered samples was studied in the temperature range of 200–1400 °C using DSC. It was found that the addition of pentavalent oxides Ta_2O_5 and Nb_2O_5 contributed to the destabilization of high temperature phases (*c* and *t*) and the formation of *m*-phase upon cooling. The *m*-phase subsequently transformed to *t*-phase upon reheating to temperatures between 500 and 700 °C. The addition of trivalent co-dopants Sc_2O_3 and Yb_2O_3 to 7YSZ effectively stabilized the *c*-phase to room temperature after sintering at 1500 °C. The *c*-phase remained stable up to 1400 °C. It was found, however, that during cooling from 1400 °C to room temperature, the *c*-phase exhibited a possible disorder to ordered transition due to defect clustering. The tetravalent CeO_2 addition to 7YSZ played a role in the stabilization of *t*-phase to room temperature and the *t*-phase was not subject to any phase transformation in the temperatures between 100 and 1400 °C. The specific heat measurement was strongly influenced by the occurrence of phase transformation. Combined with the experimental errors, the specific heat values determined in this study were not in a close agreement with the computed values based on Neumann–Kopp rule.

Acknowledgements

Financial support for this research was provided by National Science and Engineering Research Council (NSERC) of Canada. The authors also thank NSERC for the undergraduate summer scholarship awarded to Mr. Andrey Zakurdaev.

References

[1] A. Dwivedi, A.N. Cormack, Phil. Mag. A 61 (1990) 1.
[2] J. Chevalier, L. Gremillard, S. Deville, Annu. Rev. Mater. Res. 37 (2007) 1.
[3] S.M. Meier, D.K. Gupta, Trans. ASME 116 (1994) 250.
[4] P.G. Klemens, in: K.E. Wilkes (Ed.), Thermal Conductivity of Zirconia, vol. 23, Thermal Conductivity, Technomics, Lancaster, PA, 1996, pp. 209–220.
[5] J.R. Nicholls, K.J. Lawson, Surf. Coat. Technol. 151–152 (2002) 383.
[6] Y.A. Tamarin, E.B. Kachanov, S.V. Zherzdev, Mater. Sci. Forum 251–254 (1997) 949.
[7] S. Raghavan, H. Wang, W.D. Porter, R.B. Dinwiddie, M.J. Mayo, Acta Mater. 49 (2000) 169.
[8] S. Stecura, Optimization of the NiCrAl–Y/ZrO_2–$Y2O_3$ thermal barrier system, NASA Tech. Memo, 86905 (1985).
[9] X. Zhao, X. Wang, P. Xiao, Surf. Coat. Technol. 200 (20–21) (2006) 5946.
[10] U. Schulz, J. Am. Ceram. Soc. 83 (2000) 904.
[11] M.H. Li, X.F. Sun, S.K. Gong, Z.Y. Zhang, H.R. Guan, Z.Q. Hu, Surf. Coat. Technol. 176 (2004) 209.
[12] D. Zhu, R.A. Miller, Ceram. Eng. Sci. Proc. 23 (2002) 457.
[13] D. Zhu, J.A. Nesbitt, T.R. McCue, C.A. Barrett, R.A. Miller, Ceram. Eng. Sci. Proc. 23 (2002) 533.
[14] D. Michel, F. Faudot, E. Gaffet, L.J. Mazerolles, J. Am. Ceram. Soc. 76 (11) (1993) 2884.
[15] D.Y. Lee, J.-J. Kim, D.-H. Cho, J. Mater. Sci. Lett. 17 (1998) 185.
[16] M. Yashima, M. Kakihana, M. Yoshimura, Solid State Ionics 86–88 (1996) 1131.
[17] M.F.C. Ladd, R.A. Palmer, Structure Determination by X-Ray Crystallography, Plenum Press, New York, 1994.
[18] R.A. Miller, J.L. Smialek, R.G. Garlick, Advances in Ceramics Science and Technology of Zirconia I, vol. 3, American Ceramic Society, Columbus, OH, 1981, pp. 241–253.
[19] Operating Instructions for DSC Apparatus: DSC 404C Pegasu, Netzsch Thermal Analysis, 1998.
[20] Dongmei Wang, PhD thesis, Carleton University, December 2006.
[21] B.-K. Jang, H. Matsubara, J. Alloy Compd. 419 (2006) 243.
[22] T. Liu, Y.-W. Mai, M.V. Swain, J. Mater. Sci. 29 (3) (1994) 835.
[23] D.Y. Lee, K.-J. Kim, D.-H. Cho, J. Mater. Sci. Lett. 17 (1998) 185.
[24] X. Huang, D.M. Wang, A. Zurkadaev, Microstructure and Phase Transformation of Zirconia-Based Ternary Oxides for Thermal Barrier Coating Applications, J. Mater. Sci. 43 (8) (2008) 2631–2641.
[25] H.G. Scott, J. Mater. Sci. 10 (1975) 1527.
[26] Y. Moriya, A. Navrotsky, J. Chem. Thermodyn. 38 (2006) 211.
[27] H.S. Maiti, K.V.G.K. Gokhale, E.C. Subbarao, J. Am. Ceram. Soc. 55 (1972) 317.
[28] A. Dwivedi, A.N. Cormack, Philos. Mag. A 61 (1990) 1.
[29] P.J. Botha, J.C.H. Chiang, J.D. Comins, P.M. Mjwara, J. Appl. Phys. 75 (11) (1993) 7268.
[30] D. Steele, B.E.F. Fender, J. Phys. C7 (1974) 1.
[31] S. Hull, T.W.D. Farley, M.A. Hackett, W. Hayes, R. Osborn, N.H. Anderson, K. Clausen, M.T. Hutchings, W.G. Stirling, Solid State Ionics 28–30 (1988) 488.
[32] P. Kountouros, G. Petzow, in: S. Badwal, M.J. Bannister, R.H.J. Hannink (Eds.), Science and Technology of Zirconia V, Technomic, Lancaster, Basel, 1993, pp. 30–48.
[33] D.-J. Kim, J. Am. Ceram. Soc. 73 (1) (1990) 115.
[34] B. Leclercq, R. Mevrel, V. Liedtke, W. Hohenauer, Mat-wiss. u. Werkstofftech 34 (2003) 406.
[35] R.A. Swain, Thermodynamics of Solids, Wiley, New York, 1972.
[36] O. Kubaschewski, C.B. Alcock, Metallurgical Thermochemistry, Pergamon Press, London, UK, 1979.
[37] Y.A. Landa, Y.A. Polonsit, B.S. Glazachev, T.V. Milovidova, Refractories 15 (2) (1974) 86.